

Spin-density wave and superconductivity in $\text{La}_4\text{Ni}_3\text{O}_{10}$ under ambient pressure

Ming Zhang,^{1,*} Hongyi Sun,^{2,3,*} Yu-Bo Liu,^{4,*} Qihang Liu,^{5,6} Wei-Qiang Chen,^{5,6,†} and Fan Yang^{4,‡}

¹*Zhejiang Key Laboratory of Quantum State Control and Optical Field Manipulation,
Department of Physics, Zhejiang Sci-Tech University, 310018 Hangzhou, China*

²*Shenzhen Institute for Quantum Science and Engineering,
Southern University of Science and Technology, Shenzhen 518055, China*

³*International Quantum Academy, Shenzhen 518048, China*

⁴*School of Physics, Beijing Institute of Technology, Beijing 100081, China*

⁵*Department of Physics and Guangdong Basic Research Center of Excellence for Quantum Science,
Southern University of Science and Technology, Shenzhen 518055, China*

⁶*Shenzhen Key Laboratory of Advanced Quantum Functional Materials and Devices,
Southern University of Science and Technology, Shenzhen 518055, China*

We investigate the spin-density wave (SDW) behavior and the potential for superconductivity (SC) in $\text{La}_4\text{Ni}_3\text{O}_{10}$ under ambient pressure using a multi-orbital random-phase approximation (RPA). Starting with a twelve-orbital tight-binding model derived from density functional theory (DFT) calculations, we explore the influence of Hubbard interactions on SDW formation. Our analysis reveals a stripe-like SDW characterized by an incommensurate wave vector, $\mathbf{Q} \approx (\pm 0.7\pi, 0)$, suggesting a possible density wave instability in agreement with recent experiments. This configuration is driven by nesting of outer-layer Ni d_{z^2} orbitals and exhibits interlayer antiferromagnetic ordering between the top and bottom NiO layers, with the middle layer serving as a node. We demonstrate that the Hund's coupling J_H is the primary driver of the observed SDW. While superconductivity is absent in the undoped system under ambient pressure, it becomes attainable with appropriate hole doping ($\delta = -0.4$), resulting in a SC gap structure similar to the high-pressure phase. Our study identifies the specific conditions for realizing the ambient pressure stripe density wave: $J_H > 0.16U$. Additionally, when doping leads to sufficient nesting at (0,0), the system's magnetic fluctuations transition into a stable Néel-type antiferromagnetic state, analogous to the high-pressure case.

I. INTRODUCTION

The discovery of superconductivity at 80 K in $\text{La}_3\text{Ni}_2\text{O}_7$ under pressure has solidified the nickelates' place within the high-temperature superconductor family[1–6]. More recently, $\text{La}_4\text{Ni}_3\text{O}_{10}$, another Ruddlesden-Popper (RP) phase compound, has been found to exhibit superconductivity under pressure, with a transition temperature (T_c) of approximately 25–30 K[7–10]. While $\text{La}_4\text{Ni}_3\text{O}_{10}$ has a lower T_c than $\text{La}_3\text{Ni}_2\text{O}_7$, it exhibits a much higher superconducting volume fraction[7], suggesting bulk superconductivity, in contrast to the filamentary behavior observed in $\text{La}_3\text{Ni}_2\text{O}_7$ [11]. Along with the earlier discovery of superconductivity in infinite-layer nickelates ($\text{Nd}_{1-x}\text{Sr}_x\text{NiO}_2$, $T_c \sim 9\text{--}15\text{ K}$)[12–15], these findings have sparked interest in the electron correlations and pairing mechanisms in nickelates[16–83]. Despite the limited number of known nickelate superconductors, their shared RP structure and T_c values comparable to those of cuprates suggest the potential of nickelates as a promising area for further exploration in high-temperature superconductivity.

Similar to cuprates and iron-based superconductors[84, 85], $\text{La}_3\text{Ni}_2\text{O}_7$ and $\text{La}_4\text{Ni}_3\text{O}_{10}$ exhibit complex competing orders, including density wave transitions and

superconductivity[86–99]. Understanding the density wave instability in these compounds is essential for elucidating the mechanism of superconductivity. At ambient pressure, both $\text{La}_3\text{Ni}_2\text{O}_7$ and $\text{La}_4\text{Ni}_3\text{O}_{10}$ display density wave transitions. In $\text{La}_3\text{Ni}_2\text{O}_7$, μSR [100, 101], NMR[102], and RIXS[20] measurements reveal a spin density wave (SDW) transition around 150 K, while optical conductivity data indicate the emergence of an energy gap below 115 K, suggesting a possible charge-related density wave transition[103–106]. In $\text{La}_4\text{Ni}_3\text{O}_{10}$, X-ray and neutron scattering studies at ambient pressure have shown the emergence of an intertwined SDW and charge density wave (CDW) on the Ni sublattice below 135 K, accompanied by an unusual metal-to-metal transition[107, 108]. These experimental findings on density waves in $\text{La}_3\text{Ni}_2\text{O}_7$ and $\text{La}_4\text{Ni}_3\text{O}_{10}$ have also sparked several theoretical studies and discussions[66, 99, 109–117].

For $\text{La}_4\text{Ni}_3\text{O}_{10}$ at ambient pressure, current theoretical studies suggest that it exhibits complex magnetic fluctuation characteristics. The outer Ni layers show stronger spin fluctuations, which may contribute to "strange metal" behavior, while the inner Ni layers display weaker spin fluctuations. These phenomena are driven by layer-dependent Hund's rule coupling and competition with crystal field splitting, influenced by electronic correlations and the hybridization of the Ni d_{z^2} and $d_{x^2-y^2}$ orbitals[114–117]. However, there is a lack of theoretical investigation into the non-commensurate wave vectors observed experimentally[107] and the specific effects of Hund's rule coupling on the magnetic fluctuation

* These three authors contributed equally to this work.

† chenwq@sustech.edu.cn

‡ yangfan.blg@bit.edu.cn

tuation characteristics.

In this study, we investigate the SDW behavior and its potential for superconductivity in ambient pressure $\text{La}_4\text{Ni}_3\text{O}_{10}$ using the random-phase approximation (RPA) approach. Starting with a twelve-orbital tight-binding (TB) model derived from density functional theory (DFT) calculations, we incorporate multi-orbital Hubbard interactions to explore the system's properties. Our RPA analysis reveals a stripe SDW characterized by a wave vector $\mathbf{Q} \approx (\pm 0.7\pi, 0)$, corresponding to the nesting vector between the α_1 -pocket and β_1 -pockets. Both pockets are dominated by contributions from the outer-layer Ni d_{z^2} orbitals. In the trilayer structure, the top and bottom layers exhibit interlayer antiferromagnetic ordering, with the middle layer acting as an SDW node. Notably, the magnetic moments of the d_{z^2} orbitals are significantly larger than those of the $d_{x^2-y^2}$ orbitals. Furthermore, we find that achieving this non-commensurate SDW wave vector requires a Hund's rule coupling $J_H > 0.16U$. Upon considering appropriate hole doping, the system is predicted to transition into a superconducting phase.

The rest of this paper is organized as follows: In Sec. II, we construct an effective TB model based on the DFT band structure. Sec. III presents our calculation of the SDW in ambient-pressure $\text{La}_4\text{Ni}_3\text{O}_{10}$ using a multi-orbital RPA method, detailing both inter-unit-cell and intra-unit-cell pattern. In Sec. IV, we compared the Fermi surface (FS) nesting and density of states (DOS) features at ambient and high pressures, analyzing the mechanisms underlying the formation of the stripe-type SDW at ambient pressure and the Néel-type SDW at high pressure. Sec. V demonstrates that appropriate hole doping can induce superconductivity at ambient pressure. A summary is given in Sec. VI together with some discussions about possible experimental implications.

II. BAND STRUCTURE AND TB MODEL

To investigate the band structure of $\text{La}_4\text{Ni}_3\text{O}_{10}$ under ambient pressure, we first perform DFT calculations using the projector-augmented wave (PAW) pseudo-potentials with the exchange–correlation of the Perdew–Burke–Ernzerhof (PBE) and the GGA+U approach, as implemented in the Vienna ab-initio Simulation Package (VASP) [118–121]. The Hubbard U is set to be 3.5 eV to account for the correlation effects of Ni-3d electrons [16]. We adopt the $P2_1/a$ crystal structure with lattice constants measured experimentally at 0 GPa [62], and relax the atomic positions until the atomic force on each atom is less than 10^{-3} eV/Å. As shown in Fig. 1(a) and (b), the low-energy electronic states mainly originate from the Ni- $3d_{z^2}$ and $3d_{x^2-y^2}$ orbitals, which allows us to construct high-quality, maximally localized Wannier representations [122] by projecting the Bloch states (with a $14 \times 14 \times 6$ k mesh) from the DFT calculations onto the Ni- $3d_{z^2}$ and $3d_{x^2-y^2}$ orbitals.

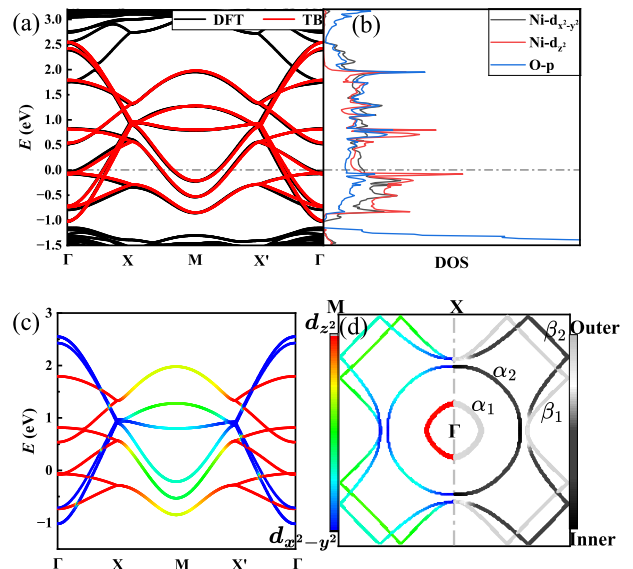


FIG. 1. (color online) Band structure of the DFT and twelve-orbital TB model for ambient pressure $\text{La}_4\text{Ni}_3\text{O}_{10}$, using experimentally refined lattice constants. (a) Comparison of the DFT band structure (black solid) and the twelve-orbital TB model (red solid) along the high-symmetry lines of $\text{La}_4\text{Ni}_3\text{O}_{10}$. (b) The DOS for various orbital components from the DFT band in (a). (c) The TB band structure corresponding to (a). (d) FS in the Brillouin zone (BZ), with the four pockets labeled. The color scheme in (c) and the left half of (d) represents the relative contributions of the d_{z^2} and $d_{x^2-y^2}$ orbital, while the colors scheme on the right half of (d) indicates the relative contributions from Ni atoms in the outer and inner layers.

The obtained TB Hamiltonian in real space can be expressed as

$$H_{\text{TB}} = \sum_{\mathbf{r}_i \Delta \mathbf{r} \mu \nu \sigma} t_{\Delta \mathbf{r} \mu \nu} c_{\mathbf{r}_i \mu \sigma}^\dagger c_{(\mathbf{r}_i + \Delta \mathbf{r}) \nu \sigma}, \quad (1)$$

Here \mathbf{r}_i represents the coordinates of site i , $\Delta \mathbf{r}_x (\Delta \mathbf{r}_y) \in (-3, 3)$ represents the hopping range. The indices $\mu, \nu = 1, \dots, 12$ containing the d_{z^2} and $d_{x^2-y^2}$ orbitals of the top-, middle- and bottom-layer Ni^A (Ni^B), and $\sigma = \uparrow, \downarrow$ labels spin. $c_{\mathbf{r}_i \mu \sigma}^\dagger (c_{\mathbf{r}_j \nu \sigma})$ creates (annihilates) a spin- σ electron in the orbital $\mu (\nu)$ at site $i (j)$. The elements of the hopping matrix $t_{\Delta \mathbf{r} \mu \nu}$ of this twelve-band tight-binding model are provided in the SM [123].

The obtained band structure for this TB model is shown in Fig. 1(c). A comparison between this band structure and the DFT one, shown in Fig. 1(a), indicates that the essential feature of the DFT results are well captured. The corresponding FS is shown in Fig. 1(d). The FS features two electron pockets, α_1 and α_2 , as well as two hole pockets, β_1 and β_2 . Both the α_1 and β_1 pockets primarily originate from the outer layer orbitals, with the α_1 pocket being entirely formed by the outer d_{z^2} orbital. The β_1 pocket consists of contributions from both the d_{z^2} and $d_{x^2-y^2}$ orbitals. In contrast, the primary orbital

components of the α_2 and β_2 pockets are predominantly derived from the inner layer $d_{x^2-y^2}$ orbitals. The overall electronic structure is in good agreement with previous ARPES experiment[8, 87, 124].

III. SDW CALCULATION USING RPA

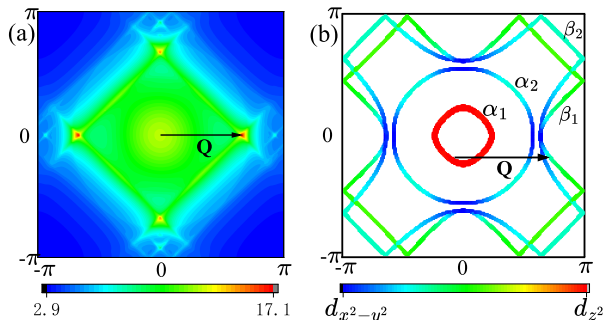


FIG. 2. (color online) (a) The distribution of the RPA-renormalized spin susceptibility $\chi^{(s)}(\mathbf{q})$ in the BZ for $U = 1.3$ eV and $J_H = 0.25U$. The maximum of the distribution is located at $\mathbf{Q} \approx (\pm 0.7\pi, 0)$. (b) FS nesting connected by the \mathbf{Q} vector. The color scheme in (b) indicates the relative contributions of the $d_{x^2-y^2}$ and d_{z^2} orbitals.

To investigate the SDW formed by electron interactions, we consider the repulsive Hubbard model described by Eq. (2):

$$H_{int} = U \sum_{i\mu} n_{i\mu\uparrow} n_{i\mu\downarrow} + V \sum_{i,\sigma,\sigma'} n_{i1\sigma} n_{i2\sigma'} + J_H \sum_{i\sigma\sigma'} \left[c_{i1\sigma}^\dagger c_{i2\sigma'}^\dagger c_{i1\sigma'} c_{i2\sigma} + (c_{i1\uparrow}^\dagger c_{i1\downarrow}^\dagger c_{i2\downarrow} c_{i2\uparrow} + h.c.) \right] \quad (2)$$

Here, U , V , and J_H denote the intra-orbital, inter-orbital Hubbard repulsion, and the Hund's rule coupling (and the pair hopping) respectively, which satisfy the relation $U = V + 2J_H$. We employ the multi-orbital RPA approach [125–131] to treat this Hamiltonian. By renormalization, the spin susceptibility $\chi^{(s)}$ and charge susceptibility $\chi^{(c)}$ can be defined as Eq. (3):

$$\begin{aligned} \chi^{(s)}(\mathbf{k}, i\nu) &= [I - \chi^{(0)}(\mathbf{k}, i\nu)U^{(s)}]^{-1} \chi^{(0)}(\mathbf{k}, i\nu), \\ \chi^{(c)}(\mathbf{k}, i\nu) &= [I + \chi^{(0)}(\mathbf{k}, i\nu)U^{(c)}]^{-1} \chi^{(0)}(\mathbf{k}, i\nu). \end{aligned} \quad (3)$$

Where $\chi^{(0)}$ is bare susceptibility for the non-interacting case, expressed as a tensor $\chi_{st}^{(0)pq}$, with p, q, s, t as orbital indices. Similarly, $\chi^{(s)}$ can be expressed as $\chi_{st}^{(s)pq}$. $U^{(s,c)}$ is the renormalized interaction strength, represented as a $12^2 \times 12^2$ matrix in this twelve-orbital system. Note that there is a critical interaction strength $U_c^{(s,c)}$ for both spin and charge susceptibilities. When $U \geq U_c^{(s,c)}$, the denominator matrix in Eq. (3) will have zero eigenvalues for certain values of \mathbf{k} , causing the renormalized spin

or charge susceptibility to diverge. This divergence indicates the onset of magnetic or charge order. When fixing $J_H = 0.25U$, we find that $U_c^{(s)} \approx 1.33$ eV. Defining $\chi^s(\mathbf{k})$ as the maximum eigenvalue of $\chi^{(s)}$ at each momentum, Fig. 2(a) shows its distribution in the BZ for $U = 1.3$ eV $< U_c^{(s)}$. Notably, the strongest spin susceptibility is located near the momentum $\mathbf{Q} \approx (\pm 0.7\pi, 0)$, which is very close to the experimentally measured value of $(\pm 0.76\pi, 0)$ [107]. At ambient conditions, $\text{La}_4\text{Ni}_3\text{O}_{10}$ crystallizes in a monoclinic structure with the space group $P_{21/a}$, which weakly breaks the D_4 symmetry and restricts the wave vector \mathbf{Q} to just two points in the first BZ. In the FS, \mathbf{Q} is the nesting vector between the α_1 -pocket and β_1 -pocket, as shown in Fig. 2(b).

The spatial distribution of the dominant spin fluctuations' intra-unit-cell modulation is illustrated in Fig. 3(a). This distribution is determined by the eigenvector corresponding to the largest eigenvalue of the spin susceptibility matrix defined as $\chi_{p,s}^{(s)} \equiv \chi_{ss}^{(s)pp}(\mathbf{k})$ with $\mathbf{k} = (\pm 0.7\pi, 0)$. As shown in Fig. 3(a), the two outer planes are out-of-phase, with the magnetic moments of Ni^A and Ni^B exhibiting a phase difference of 0.7π . The magnetic moment in the middle layer (ML) is nearly zero, indicating that the SDW has a node at the ML. In the top layer (TL) and bottom layer (BL), the magnetic moments of the d_{z^2} orbitals are significantly larger than those of the $d_{x^2-y^2}$ orbitals, which are approximately one-fifth as strong. This observation suggests that spin fluctuations primarily occur in the d_{z^2} orbitals of the two outer layers, consistent with previous DMFT calculation results[114–117].

The spin-fluctuation pattern of inter-unit-cell is determined by \mathbf{Q} . The main features of the SDW in real space can be captured by $\phi(\mathbf{r}) = \sum_{\mathbf{k}} C_z |e^{i\mathbf{k}\cdot\mathbf{r}}| \cos(\mathbf{Q}\cdot\mathbf{r})$, where $C_z = 1, 0, -1$ representing the magnetic stacking pattern along the c -axis, and the summation over \mathbf{k} is normalized by their number. The SDW has a node on the inner plane and is antiphase between the two outer planes, as shown in Fig. 3(b), which is consistent with experimentally observed features[107]. Additionally, the SDW period of $1.5a$ closely matches the experimental value[107]. This contrasts with the Néel-type SDW shown in Fig. 3(c) for high-pressure electron-doped $\text{La}_4\text{Ni}_3\text{O}_{10}$ [132].

When adjusting J_H , we find that the momentum of the strongest spin susceptibility, \mathbf{q}^c , transitions from $\mathbf{Q} \approx (\pm 0.7\pi, 0)$ to $\Gamma = (0, 0)$ as shown in Fig. 4(a). This transition is further illustrated in the distribution of $\chi^s(\mathbf{q})$ in the BZ. For $J_H = 0.1U$, as shown in Fig. 4(b), \mathbf{q}^c is located at the Γ -point. However, when $J_H = 0.3U$, \mathbf{q}^c shifts to the \mathbf{Q} -point, as shown in Fig. 4(c). To further investigate this transition, we calculated the dependence of \mathbf{q}^c on V for $J_H=0$ (Fig. 5(a)) and the dependence of \mathbf{q}^c on J_H for $V=0$ (Fig. 5(b)), excluding the commonly used relation $U = V + 2J_H$ to pinpoint the key parameter. We observe that \mathbf{q}^c remains located at Γ within the range $V \in (0, U)$, but shifts from Γ to \mathbf{Q} for $J_H > 0.16U$.

Regarding the distribution of spin fluctuations in the intra-unit-cell at $\mathbf{q}^c = (0, 0)$, our calculations reveal that

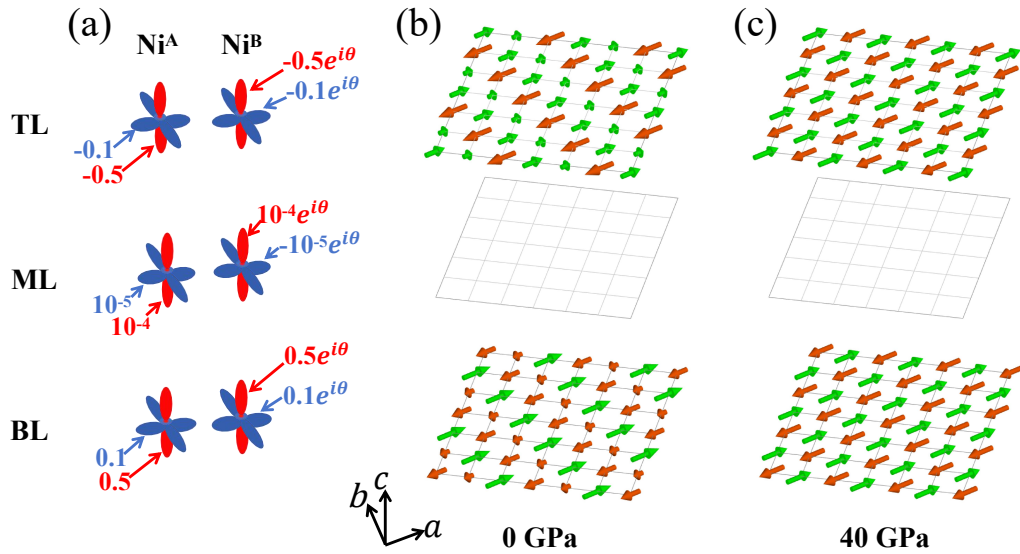


FIG. 3. (color online) (a) The leading spin-fluctuation pattern within an unit cell, where the red (blue) pattern represents the Ni- d_{z^2} ($d_{x^2-y^2}$) orbital. The trilayer is labeled as TL, ML, and BL. The numbers indicate the magnetic moment strength of the corresponding orbitals, and the phase angle of the Ni^B sublattice is $\theta = 0.7\pi$. (b) SDW model at 0 GPa plotted in the real space. (c) SDW model at 40 GPa plotted in the real space. Arrows represent the magnetic moments, with green and red indicating opposite directions. The magnitude of each magnetic moment is reflected by the arrow length. The absence of arrows in the middle layer indicates a very small magnetic moment. With SU(2) symmetry, the magnetic moments may point along the x , y , or z -axis.

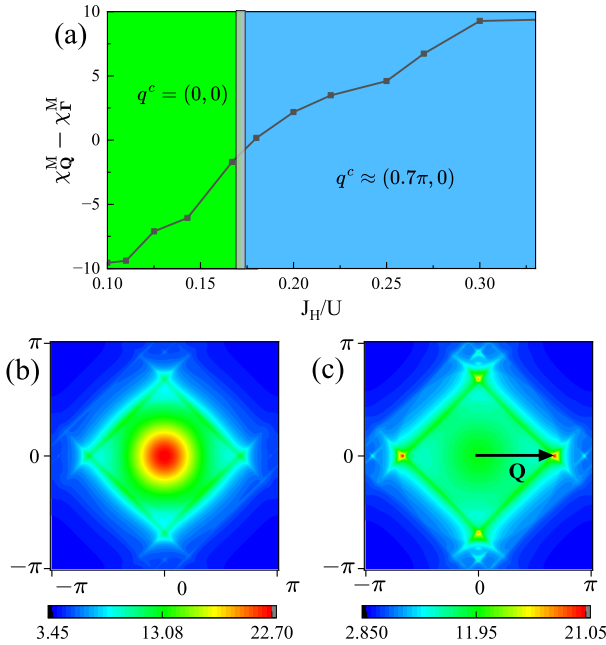


FIG. 4. (color online) (a) Dependence of $\chi_{\mathbf{Q}}^M - \chi_{\Gamma}^M$ on J_H with $U \approx U_c$. Here, $\chi_{\mathbf{Q}}^M$ and χ_{Γ}^M represent the maximum eigenvalues of χ^s at the \mathbf{Q} -point Γ -point, respectively. q^c denotes the momentum corresponding to the strongest spin susceptibility in the first BZ. When $\chi_{\mathbf{Q}}^M - \chi_{\Gamma}^M < 0$, q^c is located at the Γ -point; when $\chi_{\mathbf{Q}}^M - \chi_{\Gamma}^M > 0$, q^c is located at the \mathbf{Q} -point. (b) Distribution of $\chi^{(s)}(\mathbf{q})$ in the BZ for $J_H = 0.1U$. (c) Distribution of $\chi^{(s)}(\mathbf{q})$ in the BZ for $J_H = 0.3U$, both with $U \approx U_c$.

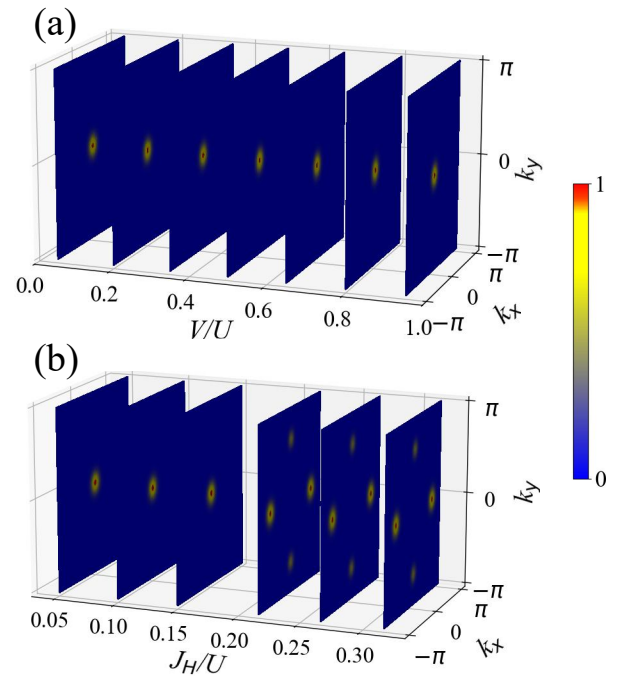


FIG. 5. (color online) Distribution of $\chi^s(\mathbf{k})$ in the BZ under different conditions. (a) Variation of $\chi^s(\mathbf{k})$ with V when $J_H = 0$, (b) Variation of $\chi^s(\mathbf{k})$ with J_H when $V = 0$. Bright spots indicate the location of q^c , and $U \approx U_c$ ensures the system is near the critical interaction strength.

the magnetic moments are predominantly localized in the two outer d_{z^2} orbitals and are antiphase between the two outer planes. The phase difference between Ni^{A} and Ni^{B} in this case is π . Notably, this configuration exhibits the same real-space SDW features as those shown in Fig. 3(c) for the high-pressure case. This indicates that for small J_H , the magnetic fluctuation resembles the Néel-type order observed under high pressure. In contrast, for $J_H > 0.16U$, the system transitions to the stripe SDW order characterized by $\mathbf{Q} \approx (\pm 0.7\pi, 0)$.

IV. COMPARISON WITH HIGH PRESSURE

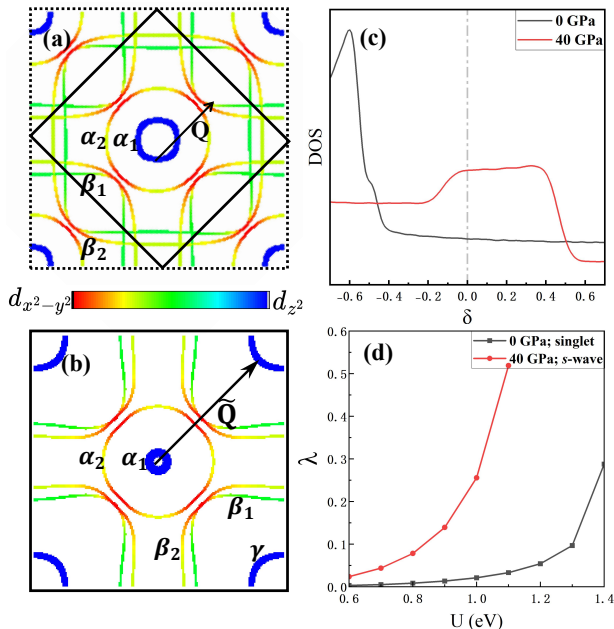


FIG. 6. (color online) Comparison between ambient and high pressure. (a) and (b) show the FS at 0 GPa and 40 GPa, respectively. The solid black line outlines the first BZ, while the area between the solid and dashed lines in (a) represents the second BZ. The color scheme in (a) and (b) indicate the relative contributions of the $d_{x^2-y^2}$ and d_{z^2} orbitals. (c) DOS, with the horizontal axis representing doping levels; the gray dashed line corresponds to the undoped case. (d) The largest pairing eigenvalue, λ , as a function of U , with $J_H = U/6$ fixed for undoped $\text{La}_4\text{Ni}_3\text{O}_{10}$. In (c) and (d), the black solid line represents the 0 GPa case, while the red solid line denotes the 40 GPa case.

There are two nesting vectors that the system tends to form: one is $\mathbf{Q} \approx (\pm 0.7\pi, 0)$ between the α_1 pocket and the β_1 pocket, while the other is near $(0,0)$. Notably, the band structure at the Γ point exhibits two nearly touching regions: the flat band bottom and flat band top, both near the Fermi level, as shown in Fig. 1(c). The flat band top forms the γ pocket at high pressure, with its flat segment located at the M point in the unfolded BZ. The nesting between the γ pocket and the α_1 pocket is (π, π) [132, 133]. After BZ folding, the flat band segment

shifts from the M point to the Γ point, meaning the (π, π) nesting vector at high pressure corresponds to the current $(0,0)$ nesting vector. The dominant nesting vector varies with J_H . When $J_H < 0.16U$, the nesting vector is $(0,0)$, while it shifts to $(\pm 0.7, 0)$ for $0.16U < J_H < 0.33U$. Based on experimental observations, at ambient pressure, the $(\pm 0.7, 0)$ nesting in $\text{La}_4\text{Ni}_3\text{O}_{10}$ predominates over the $(0,0)$ nesting.

To compare with the characteristics under high pressure, we investigated the FS nesting, DOS, and superconducting pairing strength. The FS at 0 GPa and 40 GPa are shown in Fig. 6(a) and (b), respectively. Due to the expansion of the unit cell at 0 GPa, which is $\sqrt{2} \times \sqrt{2}$ times larger than at 40 GPa, the first BZ is reduced in size. Consequently, the second BZ is also shown in (a) to clearly illustrate the folded α_1 , α_2 , β_1 and β_2 pockets. The vectors \mathbf{Q} and $\tilde{\mathbf{Q}}$ represent the dominant nesting wave vectors at 0 GPa and 40 GPa, respectively. The \mathbf{Q} vector connects the α_1 pocket and the β_1 pocket, with the α_1 pocket formed by the outer-layer d_{z^2} orbital. Although the β_1 pocket includes a mixture of the outer-layer $d_{x^2-y^2}$ and d_{z^2} orbitals, the nesting with the α_1 pocket is primarily driven by the outer-layer d_{z^2} orbital. For the $\tilde{\mathbf{Q}}$ vector, high-pressure calculations show that both the α_1 pocket and the γ pocket are associated with the outer-layer d_{z^2} orbital. Therefore, whether under high pressure or ambient pressure, the nesting vector is formed between the pockets associated with the outer-layer d_{z^2} orbitals. These nesting contribute to the SDW pattern, leading to a stripe-type SDW at ambient pressure, as shown in Fig. 3(b), and a Néel-type SDW at high pressure, as shown in Fig. 3(c).

Since the DOS at 0 GPa is lower than that at 40 GPa when doping is zero, as shown in Fig. 6(c), it is not surprising that superconductivity was initially discovered under high-pressure conditions. After performing the RPA, we used the mean-field approximation to calculate the linearized superconducting gap equation. The resulting dependence of the superconducting pairing eigenvalue λ on U is shown in Fig. 6(d). Here λ reflects the level of superconducting T_c , where a larger λ implies a higher T_c (for more details, see the next section). Compared to 40 GPa, the λ at 0 GPa is much lower, indicating that it is difficult to experimentally detect superconductivity in undoped $\text{La}_4\text{Ni}_3\text{O}_{10}$ at ambient pressure.

V. SUPERCONDUCTIVITY INDUCED BY DOPING

To investigate whether ambient pressure can achieve an appropriate superconducting T_c , we consider the doped case. In the undoped scenario, the number of electrons per unit cell is $n = 8$. We vary the electron count to $n \in (7.3, 8.7)$, corresponding to $\delta \in (-0.7, 0.7)$. The doping-dependent of DOS is shown in Fig. 6(c). In the range of $(-0.4, 0.4)$, the DOS at ambient pressure is consistently lower than that at high pressure. Upon

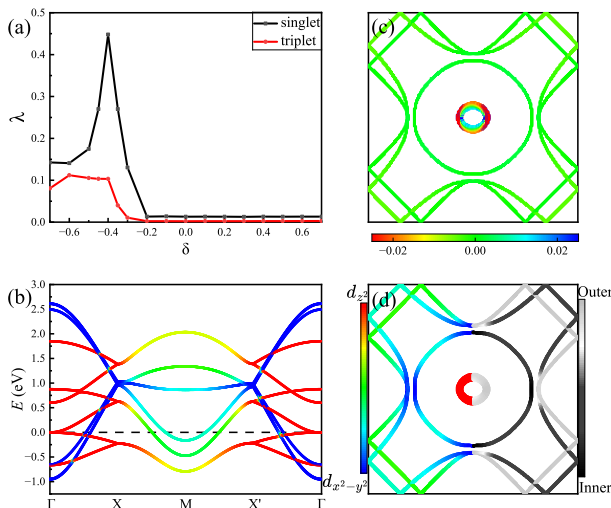


FIG. 7. (color online) Doping effects at ambient pressure. (a) The largest pairing eigenvalues λ as a function of doping, with fixed $J_H = U/6$ for $\text{La}_4\text{Ni}_3\text{O}_{10}$ at 0 GPa. The black solid line represents the singlet pairing state, while the red solid line represents the triplet pairing state. (b) Band structure of $\delta = -0.4$. (c) Distribution of the dominant gap at the FS for $\delta = -0.4$. (d) FS of $\delta = -0.4$.

further hole doping at $\delta = -0.4$, the DOS at ambient pressure begins to rise significantly, eventually surpassing the high-pressure DOS and reaching a peak at $\delta = -0.6$.

After applying the RPA, we rewrite the interaction in Eq. (2) as an effective interaction $V(\mathbf{k}, \mathbf{q})$. While the mean-field method could be used directly to solve the linearized gap equation for $V(\mathbf{k}, \mathbf{q})$ and determine the leading pairing symmetry and superconducting T_c , we choose to use a thin-shell approach for computational convenience. This leads to the following eigenvalue problem of $V(\mathbf{k}, \mathbf{q})$ as:

$$-\frac{1}{(2\pi)^2} \sum_{\beta} \oint_{FS} dq_{\parallel} \frac{V^{\alpha\beta}(\mathbf{k}, \mathbf{q})}{v_F^{\beta}(\mathbf{q})} \Delta_{\beta}(\mathbf{q}) = \lambda \Delta_{\alpha}(\mathbf{k}) \quad (4)$$

Here, $\Delta_{\alpha}(\mathbf{k})$ represents the relative gap function on the α -th FS patch near T_c , and the eigenvalue λ is related to T_c through $\lambda^{-1} = \ln\left(1.13 \frac{\hbar\omega_D}{k_B T_c}\right)$. The leading pairing symmetry is determined by the largest eigenvalue λ . To facilitate an effective comparison with the high-pressure scenario, we set $U = 1$ eV and $J_H = U/6$, following Ref. [132], and then calculated the dependence of λ on doping δ , as shown in Fig. 7(a). It is evident that singlet pairing is always favored over triplet pairing. When $\delta > -0.2$, the system exhibits a measurable λ , and at $\delta = -0.4$, λ reaches its maximum of approximately 0.45. Combining this with the high-pressure results in Fig. 6(d) indicates that the λ at this doping is comparable to that under high pressure, suggesting that doping at $\delta = -0.4$ can achieve superconductivity at ambient pressure.

At $\delta = -0.4$, the Fermi level drops to the nearly touching point of the flat band bottom and top near the Γ

point, as shown in Fig. 7(b). This configuration likely optimizes the nesting around the Γ point, with the nesting vector being $(0,0)$, allowing λ to reach its peak at this doping level. Interestingly, under high pressure, this nesting vector transforms into (π, π) , connecting the α_1 pocket and the γ pocket, as shown in Fig. 6(b). Current theoretical calculations under high pressure suggest that the superconducting gap is primarily distributed in these two pockets [132, 133]. Additionally, we examined cases with larger J_H . For $J_H = 0.25U$ and $J_H = 0.3U$, the nesting vector remained fixed at $(0,0)$, indicating that the nesting between the α_1 pocket and the γ pocket remains robust despite the increase in J_H .

The distribution of the relative gap function on the FS is shown in Fig. 7(c). Under high pressure, the system exhibits D_4 symmetry, which permits potential pairing symmetries such as s -wave, d_{xy} -wave, $d_{x^2-y^2}$ -wave and degenerate (p_x, p_y) -wave states. At ambient pressure, however, the D_4 symmetry is slightly broken, reducing it to D_2 symmetry. As a result, the possible superconducting pairing symmetries are limited to singlet and triplet states. The gap shown in Fig. 7(c) exhibits singlet symmetry, consistent with the dominance of the singlet λ observed in Fig. 7(a). The superconducting gap is primarily concentrated in α_1 pocket. As shown in Fig. 7(d), this pocket is composed of pure outer-layer d_{z^2} orbitals, consistent with the reported characteristics of the superconducting gap distribution in high-pressure $\text{La}_4\text{Ni}_3\text{O}_{10}$ [132, 133].

VI. CONCLUSION

Adopting the TB model fitted from the DFT band structure, we investigated the SDW and potential superconductivity of $\text{La}_4\text{Ni}_3\text{O}_{10}$ at ambient pressure using the RPA approach. We obtain a SDW pattern consistent with experimental observations, primarily driven by Hund's coupling. This conclusion is supported by comparisons with results obtained under reduced Hund's coupling. When $J_H > 0.16$, the system exhibits a stripe SDW pattern, characterized by in-plane antiferromagnetism with a wave vector $(\pm 0.7\pi, 0)$ and antiphase antiferromagnetic ordering between the two outer layers.

This stripe SDW arises primarily from the magnetic moments in the two outer d_{z^2} orbitals, with the top and bottom layers adopting an interlayer antiferromagnetic configurations, while the middle layer serves as an SDW node. The wave vector $(\pm 0.7\pi, 0)$ corresponds to the nesting vector connecting the α_1 pocket and the β_1 pocket. In the undoped case, the $(0,0)$ nesting vector—equivalent to (π, π) in the unfolded high-pressure BZ—is suppressed by J_H .

With $\delta = -0.4$ hole doping, the system transitions into a superconducting phase. Notably, both ambient- and high-pressure superconductivity share a key characteristic: the two pockets connected by nesting are formed by pure outer-layer d_{z^2} orbitals. Furthermore, this nesting is

remarkably stable and remains unaffected by J_H . Since the eigenvalue $\lambda \approx 0.45$ at this doping exceeds the high-pressure value of $\lambda = 0.25$, we anticipate that hole doping will induce superconductivity in $\text{La}_4\text{Ni}_3\text{O}_{10}$ at ambient pressure, with T_c at $\delta = -0.4$ expected to surpass that at high pressure.

ACKNOWLEDGMENTS

We are grateful to the discussions with Chen Lu. This work is supported by the NSFC un-

der Grant Nos.12234016, 12074031, 12141402, and 12334002, Guangdong province (2020KCXTD001), Shenzhen Science and Technology Program under Grant No. RCJC20221008092722009. W.-Q. Chen is supported by the National Key R&D Program of China (Grants No. 2022YFA1403700), the Science, Technology and Innovation Commission of Shenzhen Municipality (No. ZDSYS20190902092905285), and Center for Computational Science and Engineering of Southern University of Science and Technology.

-
- [1] H. Sun, M. Huo, X. Hu, J. Li, Z. Liu, Y. Han, L. Tang, Z. Mao, P. Yang, B. Wang, J. Cheng, D.-X. Yao, G.-M. Zhang, and M. Wang, Signatures of superconductivity near 80k in a nickelate under high pressure, *Nature* **621**, 493 (2023).
- [2] Y. Zhang, D. Su, Y. Huang, Z. Shan, H. Sun, M. Huo, K. Ye, J. Zhang, Z. Yang, Y. Xu, Y. Su, R. Li, M. Smidman, M. Wang, L. Jiao, and H. Yuan, High-temperature superconductivity with zero resistance and strange-metal behaviour in $\text{La}_3\text{Ni}_2\text{O}_{7-\delta}$, *Nat. Phys.* **20**, 1269 (2024).
- [3] J. Hou, P.-T. Yang, Z.-Y. Liu, J.-Y. Li, P.-F. Shan, L. Ma, G. Wang, N.-N. Wang, H.-Z. Guo, J.-P. Sun, Y. Uwatoko, M. Wang, G.-M. Zhang, B.-S. Wang, and J.-G. Cheng, Emergence of high-temperature superconducting phase in pressurized $\text{La}_3\text{Ni}_2\text{O}_7$ crystals, *Chin. Phys. Lett.* **40**, 117302 (2023).
- [4] G. Wang, N. N. Wang, X. L. Shen, J. Hou, L. Ma, L. F. Shi, Z. A. Ren, Y. D. Gu, H. M. Ma, P. T. Yang, Z. Y. Liu, H. Z. Guo, J. P. Sun, G. M. Zhang, S. Calder, J.-Q. Yan, B. S. Wang, Y. Uwatoko, and J.-G. Cheng, Pressure-induced superconductivity in polycrystalline $\text{La}_3\text{Ni}_2\text{O}_7$, *Phys. Rev. X* **14**, 011040 (2024).
- [5] G. Wang, N. Wang, Y. Wang, L. Shi, X. Shen, J. Hou, H. Ma, P. Yang, Z. Liu, H. Zhang, X. Dong, J. Sun, B. Wang, K. Jiang, J. Hu, Y. Uwatoko, and J. Cheng, Observation of high-temperature superconductivity in the high-pressure tetragonal phase of $\text{La}_2\text{PrNi}_2\text{O}_{7-\delta}$, *arXiv preprint arXiv:2311.08212* (2023).
- [6] M. Zhang, C. Pei, Q. Wang, Y. Zhao, C. Li, W. Cao, S. Zhu, J. Wu, and Y. Qi, Effects of pressure and doping on ruddlesden-popper phases $\text{La}_{n+1}\text{Ni}_n\text{O}_{3n+1}$, *J. Mater. Sci. Technol.* **185**, 147 (2024).
- [7] Y. Zhu, D. Peng, E. Zhang, B. Pan, X. Chen, L. Chen, H. Ren, F. Liu, Y. Hao, N. Li, *et al.*, Superconductivity in pressurized trilayer $\text{La}_4\text{Ni}_3\text{O}_{10-\delta}$ single crystals, *Nature* **631**, 531 (2024).
- [8] M. Zhang, C. Pei, X. Du, Y. Cao, Q. Wang, J. Wu, Y. Li, Y. Zhao, C. Li, W. Cao, *et al.*, Superconductivity in trilayer nickelate $\text{La}_4\text{Ni}_3\text{O}_{10}$ under pressure, *arXiv preprint arXiv:2311.07423* (2023).
- [9] X. Huang, H. Zhang, J. Li, M. Huo, J. Chen, Z. Qiu, P. Ma, C. Huang, H. Sun, and M. Wang, Signature of superconductivity in pressurized trilayer-nickelate $\text{Pr}_4\text{Ni}_3\text{O}_{10-\delta}$, *arXiv preprint arXiv:2410.07861* (2024).
- [10] Q. Li, Y.-J. Zhang, Z.-N. Xiang, Y. Zhang, X. Zhu, and H.-H. Wen, Signature of superconductivity in pressurized $\text{La}_4\text{Ni}_3\text{O}_{10}$, *Chin. Phys. Lett.* **41**, 017401 (2024).
- [11] Y. Zhou, J. Guo, S. Cai, H. Sun, P. Wang, J. Zhao, J. Han, X. Chen, Q. Wu, Y. Ding, M. Wang, T. Xiang, H. kwang Mao, and L. Sun, Investigations of key issues on the reproducibility of high-Tc superconductivity emerging from compressed $\text{La}_3\text{Ni}_2\text{O}_7$, *arXiv preprint arXiv:2311.12361* (2023).
- [12] D. Li, K. Lee, B. Y. Wang, M. Osada, S. Crossley, H. R. Lee, Y. Cui, Y. Hikita, and H. Y. Hwang, Superconductivity in an infinite-layer nickelate, *Nature* **572**, 624 (2019).
- [13] K. Lee, B. Y. Wang, M. Osada, B. H. Goodge, T. C. Wang, Y. Lee, S. Harvey, W. J. Kim, Y. Yu, C. Murthy, *et al.*, Linear-in-temperature resistivity for optimally superconducting (Nd, Sr) NiO_2 , *Nature* **619**, 288 (2023).
- [14] Y. Nomura and R. Arita, Superconductivity in infinite-layer nickelates, *Rep. Prog. Phys.* **85**, 052501 (2022).
- [15] Q. Gu and H.-H. Wen, Superconductivity in nickel-based 112 systems, *The Innovation* **3** (2022).
- [16] J. Yang, H. Sun, X. Hu, Y. Xie, T. Miao, H. Luo, H. Chen, B. Liang, W. Zhu, G. Qu, *et al.*, Orbital-dependent electron correlation in double-layer nickelate $\text{La}_3\text{Ni}_2\text{O}_7$, *Nat. Commun.* **15**, 4373 (2024).
- [17] L. Wang, Y. Li, S. Xie, F. Liu, H. Sun, C. Huang, Y. Gao, T. Nakagawa, B. Fu, B. Dong, Z. Cao, R. Yu, S. I. Kawaguchi, H. Kadobayashi, M. Wang, C. Jin, H. kwang Mao, and H. Liu, Structure responsible for the superconducting state in $\text{La}_3\text{Ni}_2\text{O}_7$ at low temperature and high pressure conditions, *arXiv preprint arXiv:2311.09186* (2023).
- [18] T. Cui, S. Choi, T. Lin, C. Liu, G. Wang, N. Wang, S. Chen, H. Hong, D. Rong, Q. Wang, Q. Jin, J.-O. Wang, L. Gu, C. Ge, C. Wang, J. G. Cheng, Q. Zhang, L. Si, K. Juan Jin, and E.-J. Guo, Strain mediated phase crossover in Ruddlesden Popper nickelates, *arXiv preprint arXiv:2311.13228* (2023).
- [19] X. Sui, X. Han, X. Chen, L. Qiao, X. Shao, and B. Huang, Electronic properties of nickelate superconductor $\text{R}_3\text{Ni}_2\text{O}_7$ with oxygen vacancies, *arXiv preprint arXiv:2312.01271* (2023).
- [20] X. Chen, J. Choi, Z. Jiang, J. Mei, K. Jiang, J. Li, S. Agrestini, M. Garcia-Fernandez, X. Huang, H. Sun, D. Shen, M. Wang, J. Hu, Y. Lu, K.-J. Zhou, and D. Feng, Electronic and magnetic excitations in $\text{La}_3\text{Ni}_2\text{O}_7$, *arXiv preprint arXiv:2401.12657* (2024).

- [21] Z. Luo, X. Hu, M. Wang, W. Wú, and D.-X. Yao, Bilayer two-orbital model of $\text{La}_3\text{Ni}_2\text{O}_7$ under pressure, *Phys. Rev. Lett.* **131**, 126001 (2023).
- [22] Y. Zhang, L.-F. Lin, A. Moreo, and E. Dagotto, Electronic structure, dimer physics, orbital-selective behavior, and magnetic tendencies in the bilayer nickelate superconductor $\text{La}_3\text{Ni}_2\text{O}_7$ under pressure, *Phys. Rev. B* **108**, L180510 (2023).
- [23] Q.-G. Yang, D. Wang, and Q.-H. Wang, Possible S_{\pm} -wave superconductivity in $\text{La}_3\text{Ni}_2\text{O}_7$, *Phys. Rev. B* **108**, L140505 (2023).
- [24] F. Lechermann, J. Gondolf, S. Bötzel, and I. M. Eremin, Electronic correlations and superconducting instability in $\text{La}_3\text{Ni}_2\text{O}_7$ under high pressure, *Phys. Rev. B* **108**, L201121 (2023).
- [25] H. Sakakibara, N. Kitamine, M. Ochi, and K. Kuroki, Possible high T_c superconductivity in $\text{La}_3\text{Ni}_2\text{O}_7$ under high pressure through manifestation of a nearly half-filled bilayer hubbard model, *Phys. Rev. Lett.* **132**, 106002 (2024).
- [26] Y. Gu, C. Le, Z. Yang, X. Wu, and J. Hu, Effective model and pairing tendency in bilayer Ni-based superconductor $\text{La}_3\text{Ni}_2\text{O}_7$, *arXiv preprint arXiv:2306.07275* (2023).
- [27] Y. Shen, M. Qin, and G.-M. Zhang, Effective bilayer model hamiltonian and density-matrix renormalization group study for the high- T_c superconductivity $\text{La}_3\text{Ni}_2\text{O}_7$ under high pressure, *Chin. Phys. Lett.* **40**, 127401 (2023).
- [28] V. Christiansson, F. Petocchi, and P. Werner, Correlated electronic structure of $\text{La}_3\text{Ni}_2\text{O}_7$ under pressure, *Phys. Rev. Lett.* **131**, 206501 (2023).
- [29] D. A. Shilenko and I. V. Leonov, Correlated electronic structure, orbital-selective behavior, and magnetic correlations in double-layer $\text{La}_3\text{Ni}_2\text{O}_7$ under pressure, *Phys. Rev. B* **108**, 125105 (2023).
- [30] W. Wú, Z. Luo, D.-X. Yao, and M. Wang, Superexchange and charge transfer in the nickelate superconductor $\text{La}_3\text{Ni}_2\text{O}_7$ under pressure, *Sci. China-Phys. Mech. Astron.* **67**, 117402 (2024).
- [31] Y. Cao and Y.-f. Yang, Flat bands promoted by hund's rule coupling in the candidate double-layer high-temperature superconductor $\text{La}_3\text{Ni}_2\text{O}_7$ under high pressure, *Phys. Rev. B* **109**, L081105 (2024).
- [32] X. Chen, P. Jiang, J. Li, Z. Zhong, and Y. Lu, Critical charge and spin instabilities in superconducting $\text{La}_3\text{Ni}_2\text{O}_7$, *arXiv preprint arXiv:2307.07154* (2023).
- [33] Y.-B. Liu, J.-W. Mei, F. Ye, W.-Q. Chen, and F. Yang, s_{\pm} -wave pairing and the destructive role of apical-oxygen deficiencies in $\text{La}_3\text{Ni}_2\text{O}_7$ under pressure, *Phys. Rev. Lett.* **131**, 236002 (2023).
- [34] C. Lu, Z. Pan, F. Yang, and C. Wu, Interlayer-coupling-driven high-temperature superconductivity in $\text{La}_3\text{Ni}_2\text{O}_7$ under pressure, *Phys. Rev. Lett.* **132**, 146002 (2024).
- [35] H. Oh and Y.-H. Zhang, Type-II t - J model and shared superexchange coupling from hund's rule in superconducting $\text{La}_3\text{Ni}_2\text{O}_7$, *Phys. Rev. B* **108**, 174511 (2023).
- [36] Y. Zhang, L.-F. Lin, A. Moreo, T. A. Maier, and E. Dagotto, Structural phase transition, s_{\pm} -wave pairing, and magnetic stripe order in bilayered superconductor $\text{La}_3\text{Ni}_2\text{O}_7$ under pressure, *Nat. Commun.* **15**, 2470 (2024).
- [37] Z. Liao, L. Chen, G. Duan, Y. Wang, C. Liu, R. Yu, and Q. Si, Electron correlations and superconductivity in $\text{La}_3\text{Ni}_2\text{O}_7$ under pressure tuning, *Phys. Rev. B* **108**, 214522 (2023).
- [38] X.-Z. Qu, D.-W. Qu, J. Chen, C. Wu, F. Yang, W. Li, and G. Su, Bilayer t - J - J_{\perp} model and magnetically mediated pairing in the pressurized nickelate $\text{La}_3\text{Ni}_2\text{O}_7$, *Phys. Rev. Lett.* **132**, 036502 (2024).
- [39] Y.-f. Yang, G.-M. Zhang, and F.-C. Zhang, Interlayer valence bonds and two-component theory for high- T_c superconductivity of $\text{La}_3\text{Ni}_2\text{O}_7$ under pressure, *Phys. Rev. B* **108**, L201108 (2023).
- [40] K. Jiang, Z. Wang, and F.-C. Zhang, High temperature superconductivity in $\text{La}_3\text{Ni}_2\text{O}_7$, *Chin. Phys. Lett.* (2023).
- [41] Y. Zhang, L.-F. Lin, A. Moreo, T. A. Maier, and E. Dagotto, Trends in electronic structures and s_{\pm} -wave pairing for the rare-earth series in bilayer nickelate superconductor $R_3\text{Ni}_2\text{O}_7$, *Phys. Rev. B* **108**, 165141 (2023).
- [42] J. Huang, Z. D. Wang, and T. Zhou, Impurity and vortex states in the bilayer high-temperature superconductor $\text{La}_3\text{Ni}_2\text{O}_7$, *Phys. Rev. B* **108**, 174501 (2023).
- [43] Q. Qin and Y.-F. Yang, High- T_c superconductivity by mobilizing local spin singlets and possible route to higher T_c in pressurized $\text{La}_3\text{Ni}_2\text{O}_7$, *Phys. Rev. B* **108**, L140504 (2023).
- [44] Y.-H. Tian, Y. Chen, J.-M. Wang, R.-Q. He, and Z.-Y. Lu, Correlation effects and concomitant two-orbital s_{\pm} -wave superconductivity in $\text{La}_3\text{Ni}_2\text{O}_7$ under high pressure, *Phys. Rev. B* **109**, 165154 (2024).
- [45] R. Jiang, J. Hou, Z. Fan, Z.-J. Lang, and W. Ku, Pressure driven fractionalization of ionic spins results in cupratelike high- T_c superconductivity in $\text{La}_3\text{Ni}_2\text{O}_7$, *Phys. Rev. Lett.* **132**, 126503 (2024).
- [46] D.-C. Lu, M. Li, Z.-Y. Zeng, W. Hou, J. Wang, F. Yang, and Y.-Z. You, Superconductivity from doping symmetric mass generation insulators: Application to $\text{La}_3\text{Ni}_2\text{O}_7$ under pressure, *arXiv preprint arXiv:2308.11195* (2023).
- [47] N. Kitamine, M. Ochi, and K. Kuroki, Theoretical designing of multiband nickelate and palladate superconductors with $d^{8+\delta}$ configuration, *arXiv preprint arXiv:2308.12750* (2023).
- [48] Z. Luo, B. Lv, M. Wang, W. Wú, and D.-X. Yao, High- T_c superconductivity in $\text{La}_3\text{Ni}_2\text{O}_7$ based on the bilayer two-orbital t - J model, *npj Quantum Materials* **9**, 61 (2024).
- [49] J.-X. Zhang, H.-K. Zhang, Y.-Z. You, and Z.-Y. Weng, Strong pairing originated from an emergent \mathbb{Z}_2 berry phase in $\text{La}_3\text{Ni}_2\text{O}_7$, *Phys. Rev. Lett.* **133**, 126501 (2024).
- [50] Z. Pan, C. Lu, F. Yang, and C. Wu, Effect of rare-earth element substitution in superconducting $R_3\text{Ni}_2\text{O}_7$ under pressure, *arXiv preprint arXiv:2309.06173* (2023).
- [51] H. Sakakibara, M. Ochi, H. Nagata, Y. Ueki, H. Sakurai, R. Matsumoto, K. Terashima, K. Hirose, H. Ohta, M. Kato, Y. Takano, and K. Kuroki, Theoretical analysis on the possibility of superconductivity in the trilayer ruddlesden-popper nickelate $\text{La}_4\text{Ni}_3\text{O}_{10}$ under pressure and its experimental examination: Comparison with $\text{La}_3\text{Ni}_2\text{O}_7$, *Phys. Rev. B* **109**, 144511 (2024).
- [52] H. Lange, L. Homeier, E. Demler, U. Schollwöck, A. Bohrdt, and F. Grusdt, Pairing dome from an emergent feshbach resonance in a strongly repulsive bilayer model, *Phys. Rev. B* **110**, L081113 (2024).

- [53] B. Geisler, J. J. Hamlin, G. R. Stewart, R. G. Hennig, and P. Hirschfeld, Structural transitions, octahedral rotations, and electronic properties of $A_3Ni_2O_7$ rare-earth nickelates under high pressure, *npj Quantum Materials* **9**, 38 (2024).
- [54] H. Yang, H. Oh, and Y.-H. Zhang, Strong pairing from doping-induced feshbach resonance and second fermi liquid through doping a bilayer spin-one mott insulator: application to $La_3Ni_2O_7$, *arXiv preprint arXiv:2309.15095* (2023).
- [55] L. C. Rhodes and P. Wahl, Structural routes to stabilize superconducting $La_3Ni_2O_7$ at ambient pressure, *Phys. Rev. Mater.* **8**, 044801 (2024).
- [56] H. Lange, L. Homeier, E. Demler, U. Schollwöck, F. Grusdt, and A. Bohrdt, Feshbach resonance in a strongly repulsive bilayer model: a possible scenario for bilayer nickelate superconductors, *arXiv preprint arXiv:2309.15843* (2023).
- [57] T. Kaneko, H. Sakakibara, M. Ochi, and K. Kuroki, Pair correlations in the two-orbital hubbard ladder: Implications for superconductivity in the bilayer nickelate $La_3Ni_2O_7$, *Phys. Rev. B* **109**, 045154 (2024).
- [58] Y. Zhang, L.-F. Lin, A. Moreo, T. A. Maier, and E. Dagotto, Electronic structure, magnetic correlations, and superconducting pairing in the reduced ruddlesden-popper bilayer $La_3Ni_2O_6$ under pressure: Different role of $d_{3z^2-r^2}$ orbital compared with $La_3Ni_2O_7$, *Phys. Rev. B* **109**, 045151 (2024).
- [59] Z. Ouyang, J.-M. Wang, J.-X. Wang, R.-Q. He, L. Huang, and Z.-Y. Lu, Hund electronic correlation in $La_3Ni_2O_7$ under high pressure, *Phys. Rev. B* **109**, 115114 (2024).
- [60] G. Heier, K. Park, and S. Y. Savrasov, Competing d_{xy} and s_{\pm} pairing symmetries in superconducting $La_3Ni_2O_7$: LDA + FLEX calculations, *Phys. Rev. B* **109**, 104508 (2024).
- [61] N. Yuan, A. Elghandour, J. Arneht, K. Dey, and R. Klingeler, High-pressure crystal growth and investigation of the metal-to-metal transition of ruddlesden-popper trilayer nickelates $La_4Ni_3O_{10}$, *J. Cryst. Growth* **627**, 127511 (2024).
- [62] J. Li, C.-Q. Chen, C. Huang, Y. Han, M. Huo, X. Huang, P. Ma, Z. Qiu, J. Chen, X. Hu, *et al.*, Structural transition, electric transport, and electronic structures in the compressed trilayer nickelate $La_4Ni_3O_{10}$, *Sci. China Phys. Mech. Astron.* **67**, 117403 (2024).
- [63] Z. Fan, J.-F. Zhang, B. Zhan, D. Lv, X.-Y. Jiang, B. Normand, and T. Xiang, Superconductivity in nickelate and cuprate superconductors with strong bilayer coupling, *Phys. Rev. B* **110**, 024514 (2024).
- [64] B. Geisler, L. Fanfarillo, J. J. Hamlin, G. R. Stewart, R. G. Hennig, and P. Hirschfeld, Optical properties and electronic correlations in $La_3Ni_2O_{7-\delta}$ bilayer nickelates under high pressure, *arXiv preprint arXiv:2401.04258* (2024).
- [65] X. Wu, H. Yang, and Y.-H. Zhang, Deconfined fermi liquid to fermi liquid transition and superconducting instability, *arXiv preprint arXiv:2401.08753* (2024).
- [66] Y. Wang, K. Jiang, Z. Wang, F.-C. Zhang, and J. Hu, The electronic and magnetic structures of bilayer $La_3Ni_2O_7$ at ambient pressure, *arXiv preprint arXiv:2401.15097* (2024).
- [67] S. Bötzel, F. Lechermann, J. Gondolf, and I. M. Eremin, Theory of magnetic excitations in multilayer nickelate superconductor $La_3Ni_2O_7$, *arXiv preprint arXiv:2401.16151* (2024).
- [68] Q.-G. Yang, K.-Y. Jiang, D. Wang, H.-Y. Lu, and Q.-H. Wang, Effective model and s_{\pm} -wave superconductivity in trilayer nickelate $La_4Ni_3O_{10}$, *Phys. Rev. B* **109**, L220506 (2024).
- [69] Y. Li, X. Du, Y. Cao, C. Pei, M. Zhang, W. Zhao, K. Zhai, R. Xu, Z. Liu, Z. Li, J. Zhao, G. Li, Y. Qi, H. Guo, Y. Chen, and L. Yang, Electronic correlation and pseudogap-like behavior of high-temperature superconductor $La_3Ni_2O_7$, *Chin. Phys. Lett.* **41**, 087402 (2024).
- [70] J. Huang and T. Zhou, Interlayer pairing-induced partially gapped fermi surface in trilayer $La_4Ni_3O_{10}$ superconductors, *Phys. Rev. B* **110**, L060506 (2024).
- [71] N. Wang, G. Wang, X. Shen, J. Hou, J. Luo, X. Ma, H. Yang, L. Shi, J. Dou, J. Feng, J. Yang, Y. Shi, Z. Ren, H. Ma, P. Yang, Z. Liu, Y. Liu, H. Zhang, X. Dong, Y. Wang, K. Jiang, J. Hu, S. Calder, J. Yan, J. Sun, B. Wang, R. Zhou, Y. Uwatoko, and J. Cheng, Bulk high-temperature superconductivity in the high-pressure tetragonal phase of bilayer $La_2PrNi_2O_7$, *Nature* **634**, 579 (2024).
- [72] M. Li, Y. Wang, C. Pei, M. Zhang, N. Li, J. Guan, M. Amboage, N.-D. Adama, Q. Kong, Y. Qi, and W. Yang, Distinguishing electronic band structure of single-layer and bilayer Ruddlesden-Popper nickelates probed by in-situ high pressure X-ray absorption near-edge spectroscopy, *arXiv preprint arXiv:2410.04230* (2024).
- [73] K.-Y. Jiang, Y.-H. Cao, Q.-G. Yang, H.-Y. Lu, and Q.-H. Wang, Theory of pressure dependence of superconductivity in bilayer nickelate $La_3Ni_2O_7$, *arXiv preprint arXiv:2409.17861* (2024).
- [74] X. Zhou, W. He, Z. Zhou, K. Ni, M. Huo, D. Hu, Y. Zhu, E. Zhang, Z. Jiang, S. Zhang, S. Su, J. Jiang, Y. Yan, Y. Wang, D. Shen, X. Liu, J. Zhao, M. Wang, M. Liu, Z. Du, and D. Feng, Revealing nanoscale structural phase separation in $La_3Ni_2O_{7-\delta}$ single crystal via scanning near-field optical microscopy, *arXiv preprint arXiv:2410.06602* (2024).
- [75] G. Wang, N. Wang, T. Lu, S. Calder, J. Yan, L. Shi, J. Hou, L. Ma, L. Zhang, J. Sun, B. Wang, S. Meng, M. Liu, and J. Cheng, Chemical versus physical pressure effects on the structure transition of bilayer nickelates, *arXiv preprint arXiv:2408.09421* (2024).
- [76] C.-Q. Chen, Z. Luo, M. Wang, W. Wú, and D.-X. Yao, Trilayer multiorbital models of $La_4Ni_3O_{10}$, *Phys. Rev. B* **110**, 014503 (2024).
- [77] Y.-f. Yang, Decomposition of multilayer superconductivity with interlayer pairing, *Phys. Rev. B* **110**, 104507 (2024).
- [78] S. Ryee, N. Witt, and T. O. Wehling, Quenched pair breaking by interlayer correlations as a key to superconductivity in $La_3Ni_2O_7$, *Phys. Rev. Lett.* **133**, 096002 (2024).
- [79] X. Chen, J. Zhang, A. S. Thind, S. Sharma, H. LaBollita, G. Peterson, H. Zheng, D. P. Phelan, A. S. Botana, R. F. Klie, and J. F. Mitchell, Polymorphism in the Ruddlesden-Popper nickelate $La_3Ni_2O_7$: Discovery of a hidden phase with distinctive layer stacking, *J. Am. Chem. Soc.* **146**, 3640 (2024).
- [80] Z. Dong, M. Huo, J. Li, J. Li, P. Li, H. Sun, L. Gu, Y. Lu, M. Wang, Y. Wang, and Z. Chen, Visualiza-

- tion of oxygen vacancies and self-doped ligand holes in $\text{La}_3\text{Ni}_2\text{O}_{7-\delta}$, *Nature* **630**, 847 (2024).
- [81] C. Lu, Z. Pan, F. Yang, and C. Wu, Interplay of two E_g orbitals in superconducting $\text{La}_3\text{Ni}_2\text{O}_7$ under pressure, *Phys. Rev. B* **110**, 094509 (2024).
- [82] Q. Qin, J. Wang, and Y.-f. Yang, Frustrated superconductivity in the trilayer nickelate $\text{La}_4\text{Ni}_3\text{O}_{10}$, *arXiv preprint arXiv:2405.04340* (2024).
- [83] D.-K. Seo, W. Liang, M.-H. Whangbo, Z. Zhang, and M. Greenblatt, Electronic band structure and madelung potential study of the nickelates La_2NiO_4 , $\text{La}_3\text{Ni}_2\text{O}_7$, and $\text{La}_4\text{Ni}_3\text{O}_{10}$, *Inorg. Chem.* **35**, 6396 (1996).
- [84] N. Ichikawa, S. Uchida, J. Tranquada, T. Niemöller, P. Gehring, S.-H. Lee, and J. Schneider, Local magnetic order vs superconductivity in a layered cuprate, *Phys. Rev. Lett.* **85**, 1738 (2000).
- [85] P. Dai, Antiferromagnetic order and spin dynamics in iron-based superconductors, *Rev. Mod. Phys.* **87**, 855 (2015).
- [86] T. Xie, M. Huo, X. Ni, F. Shen, X. Huang, H. Sun, H. C. Walker, D. Adroja, D. Yu, B. Shen, L. He, K. Cao, and M. Wang, Strong interlayer magnetic exchange coupling in $\text{La}_3\text{Ni}_2\text{O}_{7-\delta}$ revealed by inelastic neutron scattering, *Sci. Bull.* **69**, 3221 (2024).
- [87] X. Du, Y. Li, Y. Cao, C. Pei, M. Zhang, W. Zhao, K. Zhai, R. Xu, Z. Liu, Z. Li, *et al.*, Correlated electronic structure and density-wave gap in trilayer nickelate $\text{La}_4\text{Ni}_3\text{O}_{10}$, *arXiv preprint arXiv:2405.19853* (2024).
- [88] M. Kakoi, T. Oi, Y. Ohshita, M. Yashima, K. Kuroki, T. Kato, H. Takahashi, S. Ishiwata, Y. Adachi, N. Hatada, T. Uda, and H. Mukuda, Multiband metallic ground state in multilayered nickelates $\text{La}_3\text{Ni}_2\text{O}_7$ and $\text{La}_4\text{Ni}_3\text{O}_{10}$ probed by ^{139}La -NMR at ambient pressure, *J. Phys. Soc. Jpn.* **93**, 053702 (2024).
- [89] T. Xie, M. Huo, X. Ni, F. Shen, X. Huang, H. Sun, H. C. Walker, D. Adroja, D. Yu, B. Shen, L. He, K. Cao, and M. Wang, Neutron scattering studies on the high- t_c superconductor $\text{La}_3\text{Ni}_2\text{O}_{7-\delta}$ at ambient pressure, *arXiv preprint arXiv:2401.12635* (2024).
- [90] H. LaBollita, V. Pardo, M. R. Norman, and A. S. Botana, Electronic structure and magnetic properties of $\text{La}_3\text{Ni}_2\text{O}_7$ under pressure: active role of the $\text{Ni-}d_{x^2-y^2}$ orbitals, *arXiv preprint arXiv:2309.17279* (2023).
- [91] T. Fukamachi, Y. Kobayashi, T. Miyashita, and M. Sato, ^{139}La NMR studies of layered perovskite systems $\text{La}_3\text{Ni}_2\text{O}_{7-\delta}$ and $\text{La}_4\text{Ni}_3\text{O}_{10}$, *J. Phys. Chem. Solids* **62**, 195 (2001).
- [92] J.-J. Feng, T. Han, J.-P. Song, M.-S. Long, X.-Y. Hou, C.-J. Zhang, Q.-G. Mu, and L. Shan, Unaltered density wave transition and pressure-induced signature of superconductivity in Nd-doped $\text{La}_3\text{Ni}_2\text{O}_7$, *Phys. Rev. B* **110**, L100507 (2024).
- [93] Y. Meng, Y. Yang, H. Sun, S. Zhang, J. Luo, M. Wang, F. Hong, X. Wang, and X. Yu, Density-wave-like gap evolution in $\text{La}_3\text{Ni}_2\text{O}_7$ under high pressure revealed by ultrafast optical spectroscopy, *arXiv preprint arXiv:2404.19678* (2024).
- [94] S. Fan, Z. Luo, M. Huo, Z. Wang, H. Li, H. Yang, M. Wang, D.-X. Yao, and H.-H. Wen, Tunneling spectra with gaplike features observed in nickelate $\text{La}_3\text{Ni}_2\text{O}_7$ at ambient pressure, *Phys. Rev. B* **110**, 134520 (2024).
- [95] Y. Chen, Y.-H. Tian, J.-M. Wang, R.-Q. He, and Z.-Y. Lu, Non-fermi liquid and antiferromagnetic correlations with hole doping in the bilayer two-orbital Hubbard model of $\text{La}_3\text{Ni}_2\text{O}_7$ at zero temperature, *arXiv preprint arXiv:2407.13737* (2024).
- [96] L.-F. Lin, Y. Zhang, N. Kaushal, G. Alvarez, T. A. Maier, A. Moreo, and E. Dagotto, Magnetic phase diagram of a two-orbital model for bilayer nickelates varying doping, *arXiv preprint arXiv:2408.05689* (2024).
- [97] M. Xu, G. C. Jose, A. Rutherford, H. Wang, S. Zhang, R. J. Cava, H. Zhou, W. Bi, and W. Xie, Pressure-induced phase transitions in bilayer $\text{La}_3\text{Ni}_2\text{O}_7$, *arXiv preprint arXiv:2410.18840* (2024).
- [98] Y. Li, Y. Cao, L. Liu, P. Peng, H. Lin, C. Pei, M. Zhang, H. Wu, X. Du, W. Zhao, K. Zhai, X. Zhang, J. Zhao, M. Lin, P. Tan, Y. Qi, G. Li, H. Guo, L. Yang, and L. Yang, Distinct ultrafast dynamics of bilayer and trilayer nickelate superconductors regarding the density-wave-like transitions, *Sci. Bull.* <https://doi.org/10.1016/j.scib.2024.10.011> (2024).
- [99] I. V. Leonov, Electronic correlations and spin-charge-density stripes in double-layer $\text{La}_3\text{Ni}_2\text{O}_7$, *arXiv preprint arXiv:2410.15298* (2024).
- [100] R. Khasanov, T. J. Hicken, D. J. Gawryluk, L. P. Sorel, S. Bötzel, F. Lechermann, I. M. Eremin, H. Luetkens, and Z. Guguchia, Pressure-induced split of the density wave transitions in $\text{La}_3\text{Ni}_2\text{O}_{7-\delta}$, *arXiv preprint arXiv:2402.10485* (2024).
- [101] K. Chen, X. Liu, J. Jiao, M. Zou, C. Jiang, X. Li, Y. Luo, Q. Wu, N. Zhang, Y. Guo, *et al.*, Evidence of spin density waves in $\text{La}_3\text{Ni}_2\text{O}_{7-\delta}$, *Phys. Rev. Lett.* **132**, 256503 (2024).
- [102] Z. Dan, Y. Zhou, M. Huo, Y. Wang, L. Nie, M. Wang, T. Wu, and X. Chen, Spin-density-wave transition in double-layer nickelate $\text{La}_3\text{Ni}_2\text{O}_7$, *arXiv preprint arXiv:2402.03952* (2024).
- [103] Z. Liu, H. Sun, M. Huo, X. Ma, Y. Ji, E. Yi, L. Li, H. Liu, J. Yu, Z. Zhang, Z. Chen, F. Liang, H. Dong, H. Guo, D. Zhong, B. Shen, S. Li, and M. Wang, Evidence for charge and spin density waves in single crystals of $\text{La}_3\text{Ni}_2\text{O}_7$ and $\text{La}_3\text{Ni}_2\text{O}_6$, *Sci. China-Phys. Mech. Astron.* **66**, 217411 (2023).
- [104] Z. Liu, M. Huo, J. Li, Q. Li, Y. Liu, Y. Dai, X. Zhou, J. Hao, Y. Lu, M. Wang, and H.-H. Wen, Electronic correlations and partial gap in the bilayer nickelate $\text{La}_3\text{Ni}_2\text{O}_7$, *Nat. Commun.* **15**, 7570 (2024).
- [105] G. Wu, J. Neumeier, and M. Hundley, Magnetic susceptibility, heat capacity, and pressure dependence of the electrical resistivity of $\text{La}_3\text{Ni}_2\text{O}_7$ and $\text{La}_4\text{Ni}_3\text{O}_{10}$, *Phys. Rev. B* **63**, 245120 (2001).
- [106] N. Gupta, R. Gong, Y. Wu, M. Kang, C. Parzyck, B. Gregory, N. Costa, R. Sutarto, S. Sarker, A. Singer, *et al.*, Anisotropic spin stripe domains in bilayer $\text{La}_3\text{Ni}_2\text{O}_7$, *arXiv preprint arXiv:2409.03210* (2024).
- [107] J. Zhang, D. Phelan, A. Botana, Y.-S. Chen, H. Zheng, M. Krogstad, S. G. Wang, Y. Qiu, J. Rodriguez-Rivera, R. Osborn, *et al.*, Intertwined density waves in a metallic nickelate, *Nat. Commun.* **11**, 6003 (2020).
- [108] S. Xu, C.-Q. Chen, M. Huo, D. Hu, H. Wang, Q. Wu, R. Li, D. Wu, M. Wang, D.-X. Yao, *et al.*, Origin of the density wave instability in trilayer nickelate $\text{La}_4\text{Ni}_3\text{O}_{10}$ revealed by optical and ultrafast spectroscopy, *arXiv preprint arXiv:2405.19161* (2024).
- [109] B. Zhang, C. Xu, and H. Xiang, Emergent spin-charge-orbital order in superconductor $\text{La}_3\text{Ni}_2\text{O}_7$, *arXiv preprint arXiv:2407.18473* (2024).
- [110] H. LaBollita, V. Pardo, M. R. Norman, and A. S.

- Botana, Assessing the formation of spin and charge stripes in $\text{La}_3\text{Ni}_2\text{O}_7$ from first-principles, [arXiv preprint arXiv:2407.14409](#) (2024).
- [111] C. Qin, K. Foyevtsova, L. Si, G. A. Sawatzky, and M. Jiang, Intertwined charge and spin density wave state of $\text{La}_3\text{Ni}_2\text{O}_7$, [arXiv preprint arXiv:2410.15649](#) (2024).
- [112] X.-W. Yi, Y. Meng, J.-W. Li, Z.-W. Liao, W. Li, J.-Y. You, B. Gu, and G. Su, Nature of charge density waves and metal-insulator transition in pressurized $\text{La}_3\text{Ni}_2\text{O}_7$, *Phys. Rev. B* **110**, L140508 (2024).
- [113] X.-S. Ni, Y. Ji, L. He, T. Xie, D.-X. Yao, M. Wang, and K. Cao, First-principles study on spin density wave in $\text{La}_2\text{PrNi}_2\text{O}_{7-\delta}$, [arXiv preprint arXiv:2407.19213](#) (2024).
- [114] Z. Huo, P. Zhang, Z. Zhang, D. Duan, and T. Cui, Electronic correlations and hund's rule coupling in trilayer nickelate $\text{La}_4\text{Ni}_3\text{O}_{10}$, [arXiv preprint arXiv:2407.00327](#) (2024).
- [115] I. V. Leonov, Electronic structure and magnetic correlations in the trilayer nickelate superconductor $\text{La}_4\text{Ni}_3\text{O}_{10}$ under pressure, *Phys. Rev. B* **109**, 235123 (2024).
- [116] P.-F. Tian, H.-T. Ma, X. Ming, X.-J. Zheng, and H. Li, Effective model and electron correlations in trilayer nickelate superconductor $\text{La}_4\text{Ni}_3\text{O}_{10}$, *J. Phys.: Condens. Matter* **36**, 355602 (2024).
- [117] J.-X. Wang, Z. Ouyang, R.-Q. He, and Z.-Y. Lu, Non-fermi liquid and hund correlation in $\text{La}_4\text{Ni}_3\text{O}_{10}$ under high pressure, *Phys. Rev. B* **109**, 165140 (2024).
- [118] G. Kresse and J. Furthmüller, Efficient iterative schemes for ab initio total-energy calculations using a plane-wave basis set, *Phys. Rev. B* **54**, 11169 (1996).
- [119] J. P. Perdew, A. Ruzsinszky, G. I. Csonka, O. A. Vydrov, G. E. Scuseria, L. A. Constantin, X. Zhou, and K. Burke, Restoring the density-gradient expansion for exchange in solids and surfaces, *Phys. Rev. Lett.* **100**, 136406 (2008).
- [120] G. Kresse and D. Joubert, From ultrasoft pseudopotentials to the projector augmented-wave method, *Phys. Rev. B* **59**, 1758 (1999).
- [121] S. L. Dudarev, G. A. Botton, S. Y. Savrasov, C. Humphreys, and A. P. Sutton, Electron-energy-loss spectra and the structural stability of nickel oxide: An LSDA+ U study, *Physical Review B* **57**, 1505 (1998).
- [122] A. A. Mostofi, J. R. Yates, Y.-S. Lee, I. Souza, D. Vanderbilt, and N. Marzari, wannier90: A tool for obtaining maximally-localised wannier functions, *Comput. Phys. Commun.* **178**, 685 (2008).
- [123] See the Supplemental Materials at ... for the hopping integrals of the TB model.
- [124] H. Li, X. Zhou, T. Nummy, J. Zhang, V. Pardo, W. E. Pickett, J. F. Mitchell, and D. S. Dessau, Fermiology and electron dynamics of trilayer nickelate $\text{La}_4\text{Ni}_3\text{O}_{10}$, *Nat. Commun.* **8**, 704 (2017).
- [125] T. Takimoto, T. Hotta, and K. Ueda, Strong-coupling theory of superconductivity in a degenerate hubbard model, *Phys. Rev. B* **69**, 104504 (2004).
- [126] K. Yada and H. Kontani, Origin of weak pseudogap behaviors in $\text{Na}_{0.35}\text{CoO}_2$: Absence of small hole pockets, *J. Phys. Soc. Jpn.* **74**, 2161 (2005).
- [127] K. Kubo, Pairing symmetry in a two-orbital hubbard model on a square lattice, *Phys. Rev. B* **75**, 224509 (2007).
- [128] S. Graser, T. Maier, P. Hirschfeld, and D. Scalapino, Near-degeneracy of several pairing channels in multi-orbital models for the Fe pnictides, *New J. Phys.* **11**, 025016 (2009).
- [129] F. Liu, C.-C. Liu, K. Wu, F. Yang, and Y. Yao, d+ id' chiral superconductivity in bilayer silicene, *Phys. Rev. Lett.* **111**, 066804 (2013).
- [130] M. Zhang, J.-J. Hao, X. Wu, and F. Yang, Lifshitz transition enhanced triplet pz-wave superconductivity in hydrogen-doped KCr_3As_3 , *Phys. Rev. B* **105**, 134509 (2022).
- [131] K. Kuroki, S. Onari, R. Arita, *et al.*, Unconventional pairing originating from the disconnected fermi surfaces of superconducting $\text{LaFeAsO}_{1-x}\text{F}_x$, *Phys. Rev. Lett.* **101** (2008).
- [132] M. Zhang, H. Sun, Y.-B. Liu, Q. Liu, W.-Q. Chen, and F. Yang, The s^\pm -wave superconductivity in the pressurized $\text{La}_4\text{Ni}_3\text{O}_{10}$, *Phys. Rev. B* **110**, L180501 (2024).
- [133] Y. Zhang, L.-F. Lin, A. Moreo, T. A. Maier, and E. Dagotto, Prediction of s^\pm -wave superconductivity enhanced by electronic doping in trilayer nickelates $\text{La}_4\text{Ni}_3\text{O}_{10}$ under pressure, *Phys. Rev. Lett.* **133**, 136001 (2024).